Journal of Alloys and Compounds 1002 (2024) 175512

Contents lists available at ScienceDirect

Journal of Alloys and Compounds

journal homepage: www.elsevier.com/locate/jalcom

Improving electrochemical sodium storage performance and insight into the sodium ion diffusion in the high-pressure polymorph β-V_2O_5

Rafael Córdoba [a,*,1], Oleksandr Dolotko [b], Alois Kuhn [a], Flaviano García-Alvarado [a,*]

[a] Departamento de Química y Bioquímica, Facultad de Farmacia, Universidad San Pablo – CEU, CEU Universities, Urbanización Montepríncipe, Boadilla del Monte, Madrid 28668, Spain

[b] Karlsruhe Institute of Technology (KIT), Institute for Applied Materials-Energy Storage Systems (IAM-ESS), Hermann-von-Helmholtz-Platz 1, Eggenstein-Leopoldshafen, Karlsruhe D-76344, Germany

ARTICLE INFO

Keywords:
Vanadium oxide
Sodium-ion cathode
Batteries
High-pressure
Performance improvement
Ionic liquid-based electrolyte

ABSTRACT

The high-pressure form of vanadium pentoxide, β-V_2O_5, possesses promising sodium storage properties, featuring reversible sodium intercalation of one Na^+ per formula unit, yielding an appealing capacity of 147 mAh g^{-1}. However, its short cycle life in conventional carbonate-based electrolytes remains a significant drawback. In this work, we demonstrate that using non-carbonate-based electrolytes markedly enhances key electrochemical performances. Additionally, reducing the particle size of β-V_2O_5 through milling significantly increases the specific capacity, particularly at high current rates. Milled V_2O_5 maintains a respectable capacity of 73 mAh g^{-1} at 1 C rate, compared to the negligible capacity observed in non-milled V_2O_5. The milling process also alters the energy storage mechanism. Interestingly, after milling, sodium diffusion coefficient (D_{Na+}) increased from 1.78 × 10^{-13} to 1.73 × 10^{-11} cm^2 s^{-1}, likely due to induced near-surface defects. Sodium storage exhibits dominant faradaic behavior at slow current rates, while, at high current rates, capacitive processes predominate. The synergy of improved sodium diffusion and additional capacitive charge storage leads to significantly improved electrochemical performance at high current rates. Furthermore, ionic liquid-based electrolytes promote long-life cycling, advancing this material toward practical application as a cathode in sodium-ion cells.

1. Introduction

Lithium-ion batteries (LIBs) are known to be the most efficient electrochemical energy storage technology available today. As a result, they are widely used in electric vehicles (EVs), portable devices, and large-scale energy applications. Limited lithium resources in the Earth's crust due to the high demand for this metal, will hinder the large-scale deployment of some important applications, such as renewable energy storage systems. This is the main reason for research on post-lithium technologies, such as sodium-ion batteries (NIBs). These batteries are cheaper due to the abundance of sodium on Earth. As a result, the last decade has seen an increase in research on materials for NIBs with improved performance [1], and some companies have started to commercialize them. Moreover, this technology has also been proposed as useful for EVs, and some major battery companies are addressing this challenge for EVs.

Some of the more relevant compounds investigated as potential cathodes for NIBs [1] are the oxides Na_xCoO_2 [2], $NaMnO_2$ [3], $Na_{0.33}V_2O_5$ [4,5] and Na_xVO_2 [6,7], the phosphates $NaFePO_4$ [8] and $Na_3V_2(PO_4)_3$ (NASICON) [9], the Prussian blue $KFe_2(CN)_6$ [10], and the fluorophosphates Na_2FePO_4F [11], Na_2CoPO_4F [12] and Na_2MnPO_4F [13]. Table 1 summarizes the main electrochemical characteristics of these compounds and some others reported in recent years.

Materials with a layered structure are of particular interest due to their ability to accommodate large ions such as Na^+ in the interlayer space. Thus, they can provide not only higher capacity, but also higher rate capability through charge storage based on intercalation pseudo-capacitance [14]. At the same time, structural distortion of the layers may occur upon sodium intercalation, what does not necessarily have a detrimental effect on electrochemical performance.

Various V_2O_5 polymorphs have been proposed as attractive cathodes for NIBs. Layered α-V_2O_5 (space group *Pmmn*), the thermodynamically

* Corresponding authors.
E-mail addresses: rafael.rojano@kit.edu (R. Córdoba), flaga@ceu.es (F. García-Alvarado).
[1] Present address: Karlsruhe Institute of Technology (KIT), Institute for Applied Materials-Energy Storage Systems (IAM-ESS), Hermann-von-Helmholtz-Platz 1, Eggenstein-Leopoldshafen, Karlsruhe D-76344, Germany

https://doi.org/10.1016/j.jallcom.2024.175512
Received 3 May 2024; Received in revised form 18 June 2024; Accepted 8 July 2024
Available online 9 July 2024

most stable form consisting of linear chains of VO_5 square-based pyramids pointing alternately up and down, sharing corners and edges [15], is not able to deliver a reversible sodium intercalation in its commercial form in the 3.0 – 1.4 V vs Na^+/Na voltage range [16]. To promote electrochemical activity, it is necessary to electrochemically transform α-V_2O_5 into the α'-NaV_2O_5 phase (by discharging down to 0.8 V vs Na^+/Na) [16] or to tailor the material to obtain derived V_2O_5 structures, such as xerogels [17] or nanosized V_2O_5 [18,19]. In any case, the electrochemical performance is rather poor, and the rapid capacity fading is ascribed to the interlayer spacing being too narrow to accommodate sodium ions. This causes the structure to collapse upon long-term sodium (de)intercalation cycling [17]. Moreover, sodium diffusion in V_2O_5 is hindered upon sodium intercalation, as inferred from the evolution of the sodium diffusion coefficient: D_{Na+} of a crystalline V_2O_5 thin film is relatively high at very low sodium ion concentration (9×10^{-12} cm^2 s^{-1}) but decreases by more than an order of magnitude (5×10^{-13} – 5×10^{-14} cm^2 s^{-1}) as *x* in $Na_xV_2O_5$ increases [20]. However, in recent years, several successful advances have been made towards V_2O_5 polymorphs as cathodes for sodium-ion batteries. For example, layered γ'-V_2O_5 shows very promising electrochemical performance after particle size reduction, delivering 120 mAh g^{-1} after 50 cycles at C/2 rate (1 Na^+ per formula unit intercalated in 2 hours) [21]. The structure of γ'-V_2O_5 (space group *Pnma*) retains the layered V_2O_5 framework with the same structural motifs as in α-V_2O_5, although puckering of the layers occurs [22]. Another interesting polymorph is layered ε'-V_2O_5, which delivers approximately 200 mAh g^{-1} after 50 cycles at C/10 rate when carbon nanotubes are used as conductive agent in the composite electrode [23]. In contrast to α- and γ'-V_2O_5, the structure of ε'-V_2O_5 (space group *C* 2/*m*) consists of VO_6 octahedra zigzag like sharing edges, resulting in corrugated layers [24]. Similar to ε'-V_2O_5, the structure of high-pressure β-V_2O_5, consists of bilayers of distorted VO_6 octahedra sharing edges. β-V_2O_5 is a versatile cathode material for hosting different metal ions, such as Li [25], Mg [26] and Na [27], with respective capacities of 250 mAh g^{-1}, 361 mAh g^{-1} and 147 mAh g^{-1}.

The theoretical sodium storage capacity of 1 Na^+/formula unit (f.u.), 147 mAh g^{-1}, reached under equilibrium conditions (Fig. S1) in the voltage range 3.6 – 2 V vs Na^+/Na is also delivered at C/20 rate [27]. The equilibrium voltage profile (Fig. S1) is characteristic of an intercalation material in which the Na ions intercalate to form distinct solid solutions separated by biphasic regions [27]. It reveals the formation of three sodium intercalated $Na_xV_2O_5$ phases with different sodium content, involving structural rearrangement of the VO_6 octahedral bilayers. During the first discharge, at ~3 V, an important structural rearrangement with a shift of the VO_6 bilayers along the *b* direction is associated with the phase transformation of β-V_2O_5 into κ-$Na_xV_2O_5$ ($0.4 \leq x \leq 0.55$) [28]. Such a transformation is beneficial because the sodium diffusion coefficient increases by an order of magnitude (from 1.8×10^{-13} cm^2 s^{-1} to 2.3×10^{-12} cm^2 s^{-1}), which is a very clear consequence of the expansion of the interplanar space involved in this phase transformation.

However, β-V_2O_5 exhibits a short cycle life, and cell failure tends to happen before completing 20 – 25 cycles in carbonate-based electrolytes. Considering the significant initial capacity of ~150 mAh g^{-1}, in this work we adopted the following strategies to improve the electrochemical performance of β-V_2O_5. Firstly, different electrolytes were tested aiming to maximize cycle life and capacity. Secondly, as-prepared β-V_2O_5 was milled to enhance particle sodiation, reduce polarization and increase the capacity at high current rate. Furthermore, a comprehensive study of the evolution of the lattice of β-V_2O_5 upon (de)intercalation of x = 1 Na^+ has been performed. In addition, in this work, we have determined the sodium diffusion coefficient at dilute conditions and the charge storage mechanisms to understand any improvements in the electrochemical behavior. The results reported here pave the way for the application of this promising compound as a positive electrode material for NIBs.

2. Experimental section

2.1. Synthesis of β-V_2O_5

Previously dried V_2O_5 (Aldrich, 99.9 %) (180°C for 18 h), was placed in a gold capsule inside a graphite tube, transferred to a belt-type press, and subjected to a high pressure, high temperature treatment (800°C and 40 kbar for 30 min) [29]. A batch of the product was milled in a vibration mill to reduce the particle size attempted to improve the electrochemical performance. The milling conditions were 15 min at 15 Hz (hereafter referred to as β-V_2O_5-1515).

2.2. Morphological and structural study

The morphological characterization of β-V_2O_5-1515 was carried out by scanning electron microscopy (SEM), using a JEOL JSM-6400 microscope. Structural characterization was performed by means of X-ray diffraction (XRD) using a high-resolution diffractometer (Bruker D8) with Cu-Kα radiation (λ = 1.5418 Å) and equipped with a LynxEye® rapid solid-state position sensitive detector (PSD). Analysis of XRD data was made using FullProf software.

2.3. Bond valence sum method (BVS)

Bond valence sum difference maps (BVS-DMs) were obtained by utilizing the BVS Mapping package incorporated in FullProf [30]. The BVS-DMs are generally used to find plausible locations for intercalated ions and to probe ion conduction pathways in inorganic materials. Thus, a three-dimensional (3D) BVS-DM calculation was performed using the crystallographic information reported for the title compound of this work, β-V_2O_5. For comparison (3D) BVS-DMs were generated for three other Na ion intercalation vanadium pentoxides, namely α-V_2O_5, γ'-V_2O_5 and ε'-V_2O_5. BVS-DM isosurfaces were obtained at $|\Delta v| = 1.4$ valence units (v.u.) for Na ions.

2.4. Electrochemical characterization

Electrochemical experiments were carried out in sodium half-cells at 25 °C. The electrodes were casted from a slurry composite consisting of 80 % w/w of active material (β-V_2O_5), 10 % w/w of Super P Timcal

Table 1
Some electrochemical features of different positive electrodes for sodium ion batteries.

Material		Theoretical capacity / mAh g^{-1}	Initial discharge capacity / mAh g^{-1}	Capacity retention mAh g^{-1}@Rate	Voltage range / V	Ref.
Transition metal oxides	$NaMnO_2$	243	185	132@C/10 at cycle 20	2 – 3.8	[3]
	$NaVO_2$	253	120	120@C/20 at cycle 15	1.2 – 2.4	[7]
	α'-NaV_2O_5	294	90	90@C/10 at cycle 20	4 – 0.8	[16]
	β-V_2O_5	147	147	110@C/20 at cycle 20	2 – 3.6	[27]
Prussian blue	$KFe_2(CN)_6$	81	100	98@C/20 at cycle 30	2 – 4	[10]
Polyanionic compounds	$NaFePO_4$	154	130	100@C/10 at cycle 50	~ 2.8	[8]
	$Na_3V_2(PO_4)_3$	118	120	110@C/10 at cycle 70	2.7 – 3.8	[9]
	Na_2FePO_4F	124	90	80@C/10 at cycle 100	2.0 – 3.8	[11]

conductive carbon and 10 % w/w of PVDF binder (Kynarflex) in N-methyl-2-pyrrolidone (NMP) (Sigma Aldrich, 99.5 %). The slurry was cast onto aluminum foil (35 μm thickness) (MTI, 99.9 %) and subsequently, dried in a vacuum oven at 80 °C overnight. The electrodes were cut into disks (12 mm diameter) with an average mass loading of ~2.5 mg of composite (1.13 mg cm^{-2}). For electrochemical tests, CR2032 coin cells were assembled in an Ar-filled glove box (H_2O and O_2 < 0.1 ppm). A disk of metallic sodium (5 mm diameter) was used as both the reference and counter electrode, while the previously described composite was used as the working electrode, both separated by a glass fiber disk used as a separator (Whatman GF/D) soaked in the electrolyte.

The electrochemical performance of β-V_2O_5 was tested in the electrolyte formulations detailed below:

a) 1 M $NaClO_4$ in EC:PC 1:1 (v/v) (ethylene carbonate and propylene carbonate). It was used as a reference in as much as the electrochemical experiments of our germinal work [27] are based on this electrolyte.
b) 1 M $NaClO_4$ in EC:PC 1:1 (v/v) with 5 % FEC (fluoroethylene carbonate) as additive.
c) 1 M $NaPF_6$ in EC:PC 1:1 (v/v).
d) NaFSI:Pyr_{13}FSI 1:9 (mol ratio) [sodium bis(fluorosulfonyl)imide: N-methyl-N-propylpyrrolidinium bis(fluorosulfonyl)imide], an ionic-liquid (IL) based electrolyte (Solvionic).

Galvanostatic discharge-charge cycling at constant C/20 and at increasing current rates were performed (> 100 cycles) in the 3.6 – 2 V range. To determine the contribution of capacitive and faradaic processes to charge storage, cyclic voltammetry experiments were performed in the 3.6 – 2 V range at different scan rates (from 0.5 to 0.005 mV s^{-1}). For the GITT (Galvanostatic Intermittent Titration Technique) experiments required for the calculation of the sodium diffusion coefficient, a current of 82.5 μA (corresponding to the C/20 rate) was applied to the cell for 30 min to achieve a 0.025 incremental change in sodium content, in the 3.6 – 2 V potential range. After each step, the cell was allowed to relax for 4 h.

Potentiostatic Electrochemical Impedance Spectroscopy (PEIS) was performed using three-electrode Swagelok® type cells with metallic sodium as the reference and the counter electrode. This setup allows the contribution of the counter electrode to be eliminated so that the impedance of the working electrode and the Warburg coefficient (and thus the diffusion coefficient) can be analyzed. Measurements were carried out on fully charged electrodes in the frequency range 1 MHz – 1 mHz with a 10 mV AC perturbation. When the potential perturbation is applied, the system responds with different physicochemical mechanisms that include charge transfer and bulk diffusion. However, due to the small amplitude of the perturbation even at low frequency, the amount of intercalated sodium is expected to be low and the diffusion coefficient is thus determined at diluted conditions. Impedance data fitting and equivalent circuit modelling were performed using Z-Fit from EC-Lab software®. All electrochemical experiments were performed using a VMP3 BioLogic multichannel battery tester equipped with an impedance channel.

The specific area, considered as the best approximation to the intercalation active area, was determined by nitrogen adsorption-desorption (BET method) experiments (Micromeritics ASAP 2020 analyzer).

2.5. Operando X-ray diffraction

Operando measurements were recorded using a setup developed at KIT in close cooperation with STOE & Cie GmbH [31,32]. The diffractometer employs an Ag-source (E = 22.123 keV, λ = 0.55942 Å) with a focusing Ge 111 monochromator. A Dectris MYTHEN 2 2 K double detector, set at a fixed distance of slightly less than the width of a module (approximately 18° of 2θ), is mounted at a radius of 130 mm from the central axis of the goniometer. Diffraction patterns were obtained in the 2θ range of 0–36°, with an effective angular resolution of 0.015° of 2θ and an acquisition time of 20 min per pattern.

The electrochemical cells used for the *operando* XRD measurements consist of 2032-type coin cells with a Kapton window (125 μm thickness of the Kapton film) for beam entrance. Electrochemical tests within the operando cells were conducted using a galvanostatic system, μAUTOLAB-FRA2, TYPE III, controlled by NOVA.

The cathode material V_2O_5 mixed with conducting super P carbon (Timcal) and polyvinylidene fluoride (PVDF) binder, respectively, at weight ratio of 7:2:1 (in total ca. 5 mg), were prepared by pressing the mixture on thin aluminum mesh (wire diameter 10 μm) within a 6 mm hole in the center. On the other hand, sodium metal anode, separated by Whatman glass fiber (G/F) and impregnated with 1 M $NaClO_4$/EC:PC electrolyte, was pressed onto a holey spacer disk. In this way, only the V_2O_5 material will be detected during the *operando* diffraction measurements.

3. Results and discussion

3.1. Structural and morphological characterization

The XRD patterns of as-prepared β-V_2O_5 and β-V_2O_5-1515 are shown in Fig. 1. The angular position of all reflections of β-V_2O_5-1515 fully matches that of as-prepared β-V_2O_5. All reflections were indexed on the basis of the monoclinic cell reported for β-V_2O_5, space group $P\,2_1/m$, yielding the following refined lattice parameters: a = 7.1209(1) Å, b = 3.5741(1) Å, c = 6.2908(1) Å and β = 90.089(38)°, in excellent agreement with previous reports on β-V_2O_5 [29]. Therefore, it is clear that no transformation to α-V_2O_5 has occurred during the milling process under these milder conditions. Additionally, the broadening of the main diffraction peaks of β-V_2O_5-1515 compared to the as-prepared sample indicates a decrease in particle size.

The reduction in particle size of β-V_2O_5 after milling is also accompanied by changes in morphology as evidenced by the SEM images shown in Fig. 2. As-prepared β-V_2O_5 consists of prisms with well-defined shape and edges with a predominant particle size of 2 – 3 μm, while milled β-V_2O_5-1515 shows granular type submicrometric crystallites (100 – 350 nm) with round edges forming agglomerates of 2 – 3 μm.

Fig. 3 shows the structure of β-V_2O_5 and, for completeness, we included the V_2O_5 polymorphs able to intercalate sodium discussed in the introduction. Bond valence sum difference maps isosurfaces have

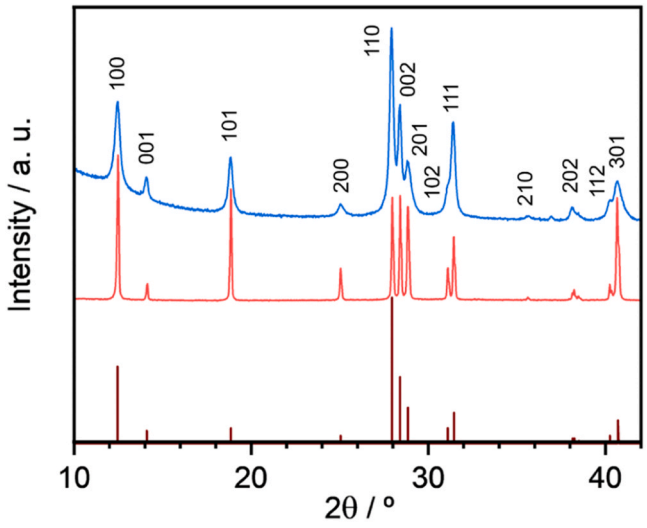

Fig. 1. Selected angular region of the XRD pattern of milled β-V_2O_5-1515 (top, blue) and as-prepared β-V_2O_5 (bottom, red). Calculated β-V_2O_5 reflections are included as a reference. The observed reflections are indexed.

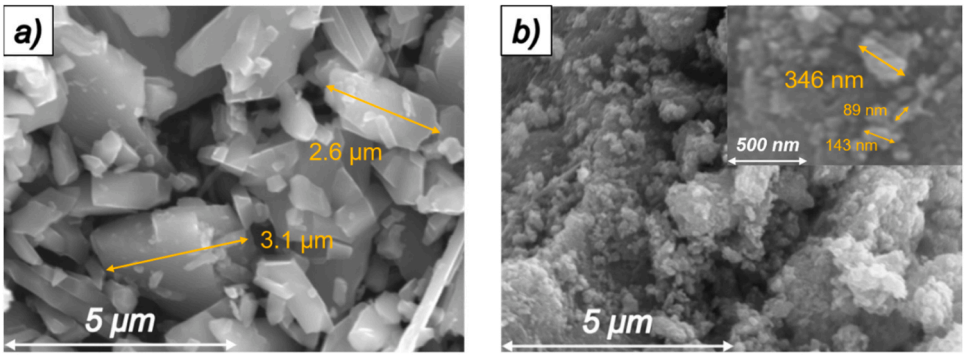

Fig. 2. SEM images showing the morphology of a) as-prepared β-V_2O_5 and b) milled β-V_2O_5-1515 (inset: detailed view of an agglomerate). The size of selected particles is shown.

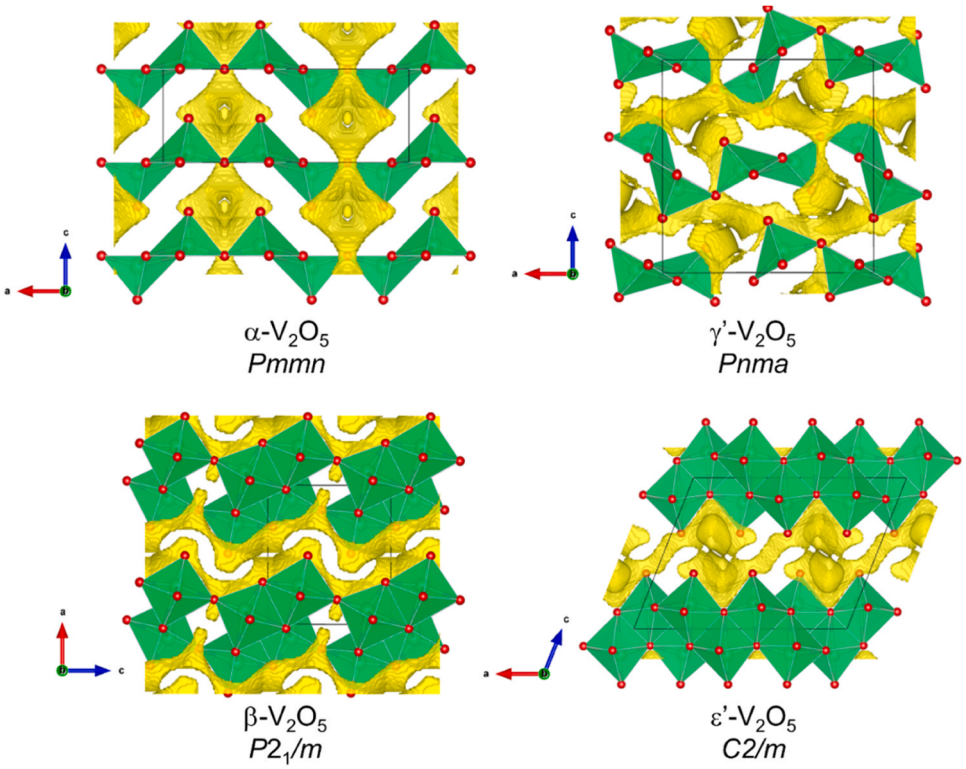

Fig. 3. Structures of different V_2O_5 forms proposed as cathodes for sodium ion batteries. VO_5 square-based pyramids and VO_6 octahedra (green), and oxygen atoms (red spheres) are shown. Three-dimensional (3D) bond valence difference map isosurfaces (yellow) for plausible Na^+ diffusion pathways with the isosurfaces of |1.4| valence units.

been calculated (BVS-DM) at $|\Delta v| = 1.4$ v.u. for Na^+ ions, which are overlapped with the corresponding crystal structures showing plausible Na^+ ion diffusion pathways in the different polymorphs.

4. Electrochemical study

4.1. Selection of different electrolytes

Galvanostatic discharge-charge profiles of cells as voltage-capacity plots for selected cycles with 1 M $NaPF_6$/EC:PC (a) and NaFSI:Pyr13FSI 1:9 (c) as the electrolyte are shown in Fig. 4. The variation in specific capacity of these same cells during cycling can be seen in Figs. 4b and 4d.

In general, the well-defined profile in 1 M $NaPF_6$/EC:PC (Fig. 4a) changes to the benefit of a sloping curve in NaFSI:Pyr_{13}FSI 1:9 (Fig. 4c) involving the same initial discharge capacity of 140 mAh g^{-1} at C/20 in both electrolytes. The well-defined large plateau near 3.2 V in 1 M $NaPF_6$/EC:PC (Fig. 4a) is shifted near 3.1 V in NaFSI:Pyr13FSI 1:9 (Fig. 4c), whereas the shorter second plateau near 2.7 V does not seem to be affected. Furthermore, the initial well-defined profile in 1 M $NaPF_6$/EC:PC is lost after only few cycles together with significant decay of capacity involving mainly the long plateau at 3.2 V (Fig. 4a), while in NaFSI:Pyr13FSI 1:9 the discharge-charge profile is well reproduced upon extended cycling (Fig. 4c). The initial decrease in capacity during the first cycles in 1 M $NaPF_6$/EC:PC (Fig. 4b), is a usual phenomenon in composite electrodes [27]. The following increase in specific capacity is ascribed to electrochemical milling [27], associated with reduction in particle size and increase in specific area of the electrode, which eventually leads to a higher sodiation rate and reduced cell polarization. However, rather limited cycle life is observed in 1 M $NaPF_6$/EC:PC and cell failure is observed after 25 cycles (Fig. 4b). Thus, no improvement in performance is achieved compared to the 1 M $NaClO_4$/EC:PC electrolyte formulation

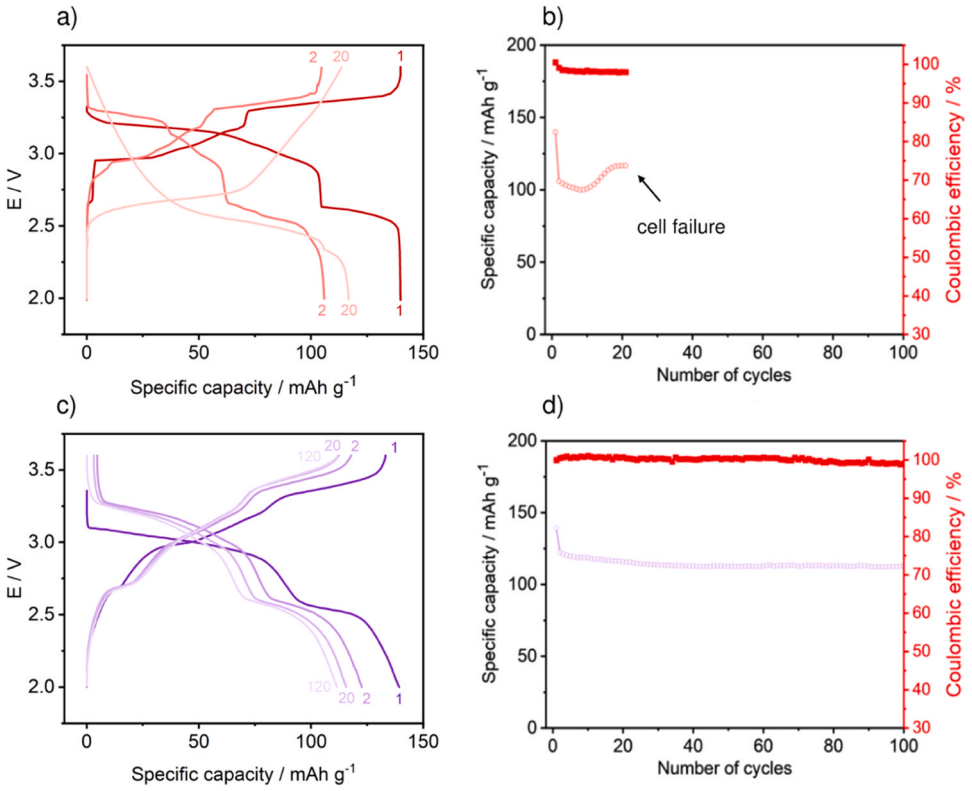

Fig. 4. Electrochemical performance at C/20 rate of sodium half-cells with β-V_2O_5 as positive electrode and 1 M $NaPF_6$/EC:PC electrolyte (a, b); and NaFSI:Pyr_{13}FSI 1:9 electrolyte (c, d).

employed in our previous work [27], with a very similar cycle life behavior (Fig. S2). The cell failure that causes the short cycle life of cells with 1 M $NaPF_6$/EC:PC and 1 M $NaClO_4$/EC:PC electrolyte is attributed to the reaction of carbonate-based solvents with the sodium negative electrode according to the immersion tests of metallic sodium in different electrolytes [33]. This assumption is supported by the fact that the type of conducting salt used does not appear to have any observable effect on cycle life of these cells. In addition, authors from ref. [33] reported that these side reactions provoke the decomposition of the PVDF binder (although they do not affect the crystal structure of the active material), which also contributes to the poor electrochemical performance of the cathode. In the same work, authors reported the use of non-carbonate-based electrolytes (for instance, IL-based electrolytes) or the incorporation of additives, such as FEC, in carbonate-based electrolytes as straightforward strategies to preventing the reaction of sodium with the electrolyte. In this case, when using carbonate-based 1 M $NaClO_4$/EC:PC electrolyte with 5 % FEC additive, cycle life is greatly prolonged (> 100 cycles), although severe capacity fade upon cycling persists (Fig. S3). We found a very significant improvement in electrochemical performance with the IL-based electrolyte NaFSI:Pyr_{13}FSI 1:9 (Fig. 4d), and not only the cycle life of the cell is widely extended, but also cycle stability is significantly improved without signs of capacity fade (75 % of capacity retention and 99.0 % of average coulombic efficiency), stabilizing at 111 mAh g^{-1} after 100 cycles at C/20 rate.

4.2. *Particle size reduction of active material*

Downsizing particle size of the active material is a common strategy to mitigate metal ion kinetic hindrance since an increased surface area with shorter sodium diffusion path length triggers faster charge storage through both intercalation and pseudocapacitive processes [14]. In this work, particle size reduction of β-V_2O_5 is realized by mechanical milling in a vibrational mill under mild conditions (Fig. 2) since β-V_2O_5 with small particle size could not be obtained from the high-pressure high-temperature synthesis process. Further reduction of particle size by higher energy milling, as for example 200 rpm for 2 h in a planetary ball mill, induces the β-V_2O_5 → α-V_2O_5 phase transformation.

To evaluate the effect that size reduction has on electrochemical performance, NaFSI:Pyr_{13}FSI 1:9 electrolyte (which yields highest capacity, best cyclability, and coulombic efficiency) is used. For sake of comparison, the same milled sample was also investigated with 1 M $NaClO_4$ in EC:PC electrolyte (the one used in our previous work) [27].

Fig. 5 shows the discharge-charge cycling behavior for sodium intercalation in as-synthesized β-V_2O_5 and milled β-V_2O_5-1515 using 1 M $NaClO_4$ in EC:PC (Figs. 5a and 5b) and NaFSI:Pyr_{13}FSI 1:9 (Figs. 5c and 5d) electrolytes at C/20 rate.

Firstly, the well-defined electrochemical profile in as-synthesized β-V_2O_5 (Figs. 5a and 5c) changes to a more sloping curve in β-V_2O_5-1515 (Figs. 5b and 5d) involving the same initial specific capacity of ca. 140 mAh g^{-1}. Particularly for carbonate-based electrolyte 1 M $NaClO_4$ in EC:PC, β-V_2O_5-1515 exhibits rather limited cycle life (Fig. 6b), similar to as-synthesized β-V_2O_5 (Fig. 6a), and cell failure appears after ca. 25 cycles. The steadily decreasing capacity of β-V_2O_5-1515 in 1 M $NaClO_4$ in EC:PC (Fig. 6b) upon cycling, different from as-synthesized β-V_2O_5 (Fig. 6a), suggests that no electrochemical milling takes place in β-V_2O_5-1515, which can be understood by the smaller size of active material, already decreased by mechanically milling.

Secondly, β-V_2O_5 and β-V_2O_5-1515 present improved cycle stability (Figs. 5c and 5d) and capacity retention (Figs. 6c and 6d) in NaFSI:Pyr_{13}FSI 1:9 electrolyte. After 120 cycles, specific capacity is better retained in β-V_2O_5-1515 (120 mAh g^{-1}, Fig. 6d) compared to as-synthesized β-V_2O_5 (111 mAh g^{-1}, Fig. 6c) Coulombic efficiency is improved after reducing the particle size, from 98.8 % for the as-prepared β-V_2O_5 to 99.5 % for the milled β-V_2O_5-1515 at cycle 120.

Fig. S4 shows the extended cycling for β-V_2O_5-1515 in NaFSI:Pyr_{13}FSI 1:9 as the electrolyte, which remarkably withstands an appealing capacity retention of 85 % and a coulombic efficiency of more than 95 % after more than 200 cycles.

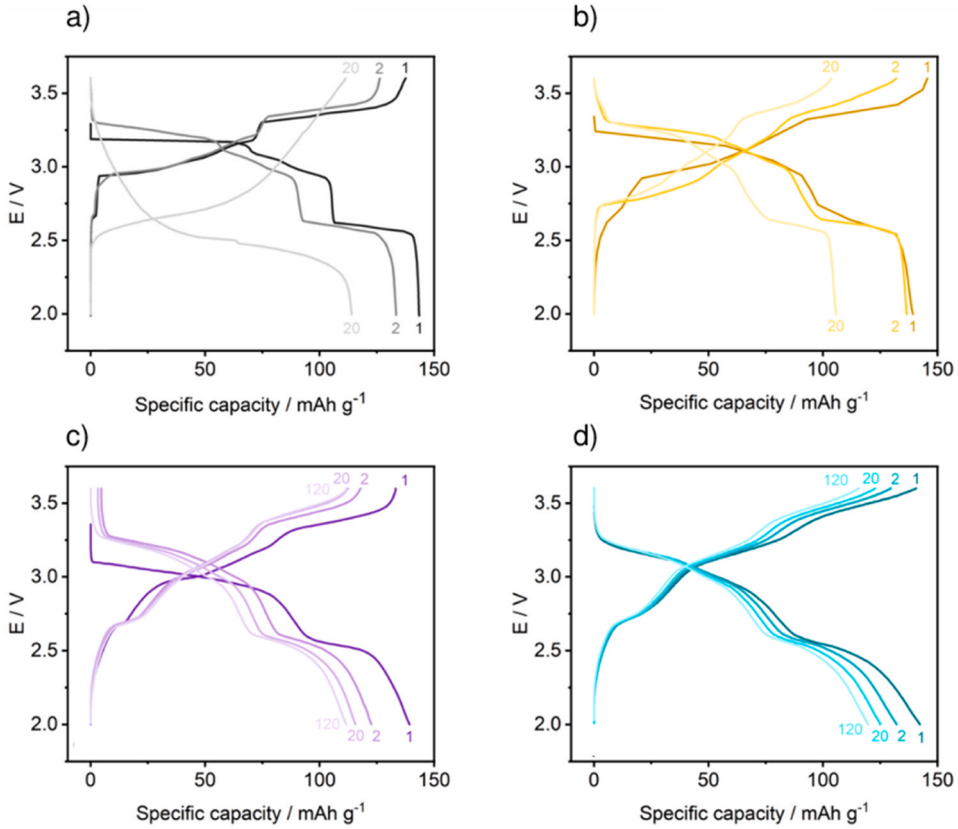

Fig. 5. Galvanostatic discharge-charge cycling at C/20 rate of selected cycles (as labelled in each figure) of sodium half-cells with the following positive electrode – electrolyte combinations: a) β-V_2O_5 – 1 M $NaClO_4$/EC:PC, b) β-V_2O_5-1515 – 1 M $NaClO_4$/EC:PC, c) β-V_2O_5 – NaFSI:Pyr_{13}FSI 1:9, d) β-V_2O_5-1515 – NaFSI:Pyr_{13}FSI 1:9.

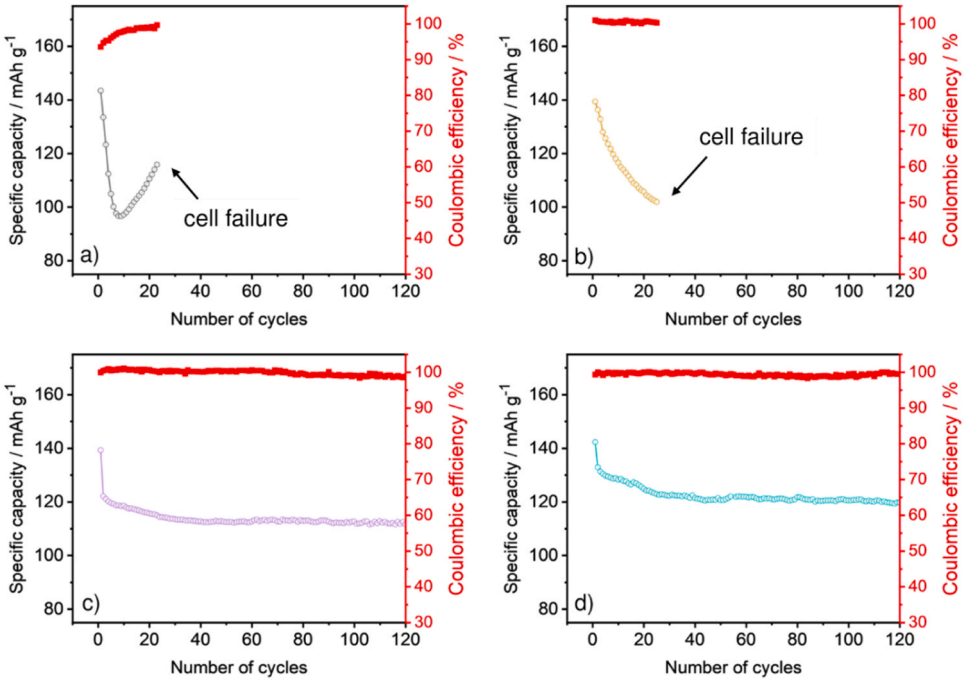

Fig. 6. Variation of the specific capacity with the number of cycles for β-V_2O_5 vs Na^+/Na cells with the following positive electrode – electrolyte combinations: a) β-V_2O_5 – 1 M $NaClO_4$/EC:PC, b) β-V_2O_5-1515 – 1 M $NaClO_4$/EC:PC, c) β-V_2O_5 – NaFSI:Pyr_{13}FSI 1:9, d) β-V_2O_5-1515 – NaFSI:Pyr_{13}FSI 1:9.

The beneficial effect of particle size reduction on the electrochemical performance of β-V_2O_5 is clearly seen at increasing C rates. Fig. 7 shows that the discharge-charge rate capability is even more improved for β-V_2O_5-1515 in NaFSI:Pyr_{13}FSI 1:9 at higher C rates compared to as-synthesized β-V_2O_5 in 1 M $NaClO_4$/EC:PC reported in our previous work [27]. At all current rates from C/20 to 1 C, β-V_2O_5-1515 in NaFSI:

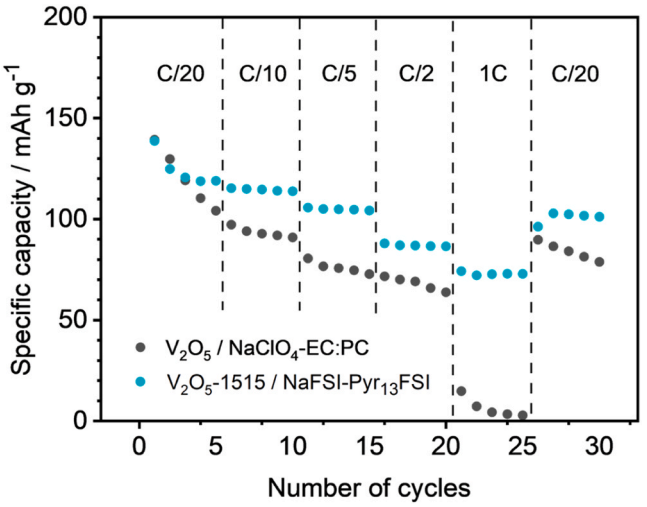

Fig. 7. Specific capacities as a function of cycle number at different, successive C/n rates of as-synthesized β-V_2O_5 in 1 M $NaClO_4$:EC:PC electrolyte (black) and β-V_2O_5-1515 in NaFSI:Pyr_{13}FSI 1:9 (blue).

Pyr_{13}FSI 1:9 shows improved cycle stability and higher capacity: 120 mAh g^{-1} vs 100 mAh g^{-1} at C/20, 115 vs 90 mAh g^{-1} at C/10 rate, 105 vs 75 mAh g^{-1} at C/5 rate and 90 vs 65 mAh g^{-1} at C/2 rate. This improvement is particularly prominent at high C rates where β-V_2O_5-1515 holds ~75 mAh g^{-1} at 1 C. This is a remarkable finding considering that the diffusion of sodium in many oxide hosts is usually rather sluggish. Fig. 8 summarizes the improved cycling of β-V_2O_5-1515 compared to as-prepared β-V_2O_5 at a higher rate of 1 C, employing the same NaFSI:Pyr_{13}FSI 1:9 electrolyte. An enhanced very stable discharge capacity of 75 mAh g^{-1} is available at 1 C rate for > 150 cycles, *i.e.* three times higher than that developed by as-synthesized β-V_2O_5.

4.3. Structural changes during the first discharge-charge process

The structural evolution of β-V_2O_5 during galvanostatic discharge-charge cycling in the 2.0 – 4.0 V potential range has been investigated by *operando* XRD. XRD patterns of β-$Na_xV_2O_5$ recorded during the first discharge-charge process under *operando* conditions as a contour map are shown in Fig. 9b along with the corresponding electrochemical curve (Fig. 9a) and XRD patterns of selected compositions (Fig. 9c). Before discharge, all reflections can be indexed based on monoclinic β-V_2O_5. As shown in Figs. 9b and 9c, during early stage of discharge (x = 0 – 0.2), the characteristic monoclinic fingerprint of the initial V_2O_5 compound is preserved. For x > 0.2, new reflections appear, and its intensity increases, while those from the Na-poor β-$Na_xV_2O_5$ phase decrease and completely disappear at x = 0.4, indicating the presence of a biphasic domain. The two-phase nature of transition from β-V_2O_5 to $Na_{0.4}V_2O_5$ is clearly visible from the disappearance of the 100 reflection of V_2O_5 at ~4.2° and simultaneous appearance of a corresponding reflection at a lower angle of 3.8°. This transition involves a significant structural rearrangement of the VO_6 bilayers, including a shift of the bilayers by *b*/2 along the crystallographic *b* direction [28], accompanied by a change in space group from *P* $2_1/m$ in V_2O_5 to *C* 2/*m* in $Na_{0.4}V_2O_5$. Since C-centering leads to doubling of the *a* parameter (Fig. 10), the interlayer distance in $Na_{0.4}V_2O_5$ is now represented by ~*a*/2 (previously ~*a* in V_2O_5). As a result of Na^+ ion intercalation, the interlayer spacing increases from 7.12 Å in V_2O_5 to 8.53 Å in $Na_{0.4}V_2O_5$, while *b* and *c* parameters undergo only minor changes (Table 2). The sodium intercalation then progresses in a solid solution from $Na_{0.4}V_2O_5$ to $Na_{0.7}V_2O_5$, with only subtle continuous angular shifts of reflections (Fig. 9b) and slight changes in lattice parameters (Fig. 10 and Table 2). The *a* parameter slightly decreases within this single phase region, likely due to some rearrangement of VO_6 bilayers caused by the coordination of Na^+ ions, while *b* and *c* parameters continue to increase. For x > 0.8, new reflections emerge and intensify, while those from β-$Na_{0.7}V_2O_5$ gradually decrease and eventually disappear, indicating the presence of a second biphasic domain. These new diffraction peaks can also be indexed with a monoclinic cell (*C* 2/*m* space group). However, as evidenced by the position of the 200 reflections at a lower 2θ value (3.8° in $Na_{0.7}V_2O_5$ vs. 3.2° in NaV_2O_5), the sodium-rich NaV_2O_5 phase exhibits a larger *a* parameter (19.5 Å vs. 17.0 Å) with the larger interlayer spacing of 9.54 Å vs. 8.34 Å (Table 2) to accommodate increasing amounts of sodium ions leading to the fully sodiated β-NaV_2O_5 compound. Upon charging, all reflections recover to their initial positions through the same phase domains detected during discharge (Fig. 9b), confirming the full reversibility of the sodium (de)intercalation process. Table 2 lists the refined lattice parameters of selected sodiated $Na_xV_2O_5$ phases (x = 0, 0.4, 0.7 and 1) during discharge and charge as determined from the fitting of the XRD patterns shown in Fig. 9c. The detailed evolution of the lattice parameters as a function of sodium uptake x in $Na_xV_2O_5$ is shown in Fig. 10.

4.4. Charge storage mechanism in as-prepared and milled β-V_2O_5

Since the increase in capacity and better rate capability upon particle size reduction may be due to either improved intercalation kinetics (decreasing diffusion paths promoting full sodiation of particles) or a change in the charge storage mechanism, the faradaic and surface processes contributions to the charge storage mechanism were further investigated by CV performed at different scan rates (Fig. 11). Fig. 11a collects scans from 0.5 to 0.005 mV s^{-1} in as-synthesized β-V_2O_5, while the profile of the capacitive current contribution is shown in Figs. 11b and 11c for 0.02 and 0.5 mV s^{-1}, respectively, which allows a comparison of the contributions at low and high scan rates (the calculation procedure is described in the Supporting Information, Fig. S5 and

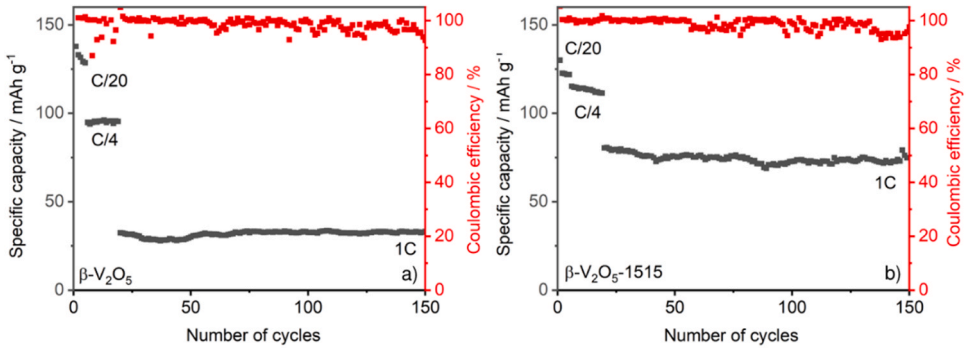

Fig. 8. Specific capacity as a function of number of cycles for a) as-prepared β-V_2O_5 and b) β-V_2O_5-1515 at 1 C rate. IL-based electrolyte NaFSI:Pyr_{13}FSI 1:9 was employed in both cells. 5 cycles at C/20 rate and 20 cycles at C/4 rate were performed as a preconditioning step.

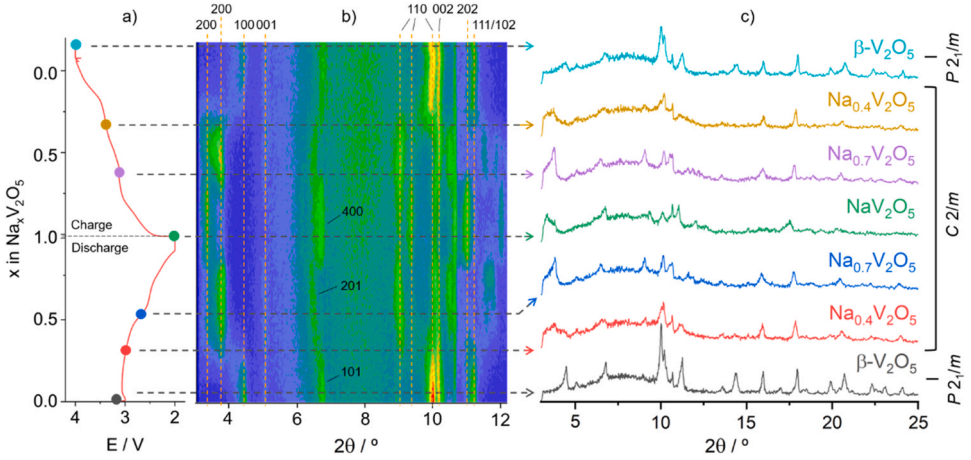

Fig. 9. Contour map of *operando* X-ray diffraction of β-V_2O_5 collected during a full discharge-charge cycle (b), the corresponding discharge-charge profile at C/20 in the cell voltage range of 2.0 – 4.0 V vs. Na^+/Na (a) and selected XRD patterns of $Na_xV_2O_5$ with different sodium content (c).

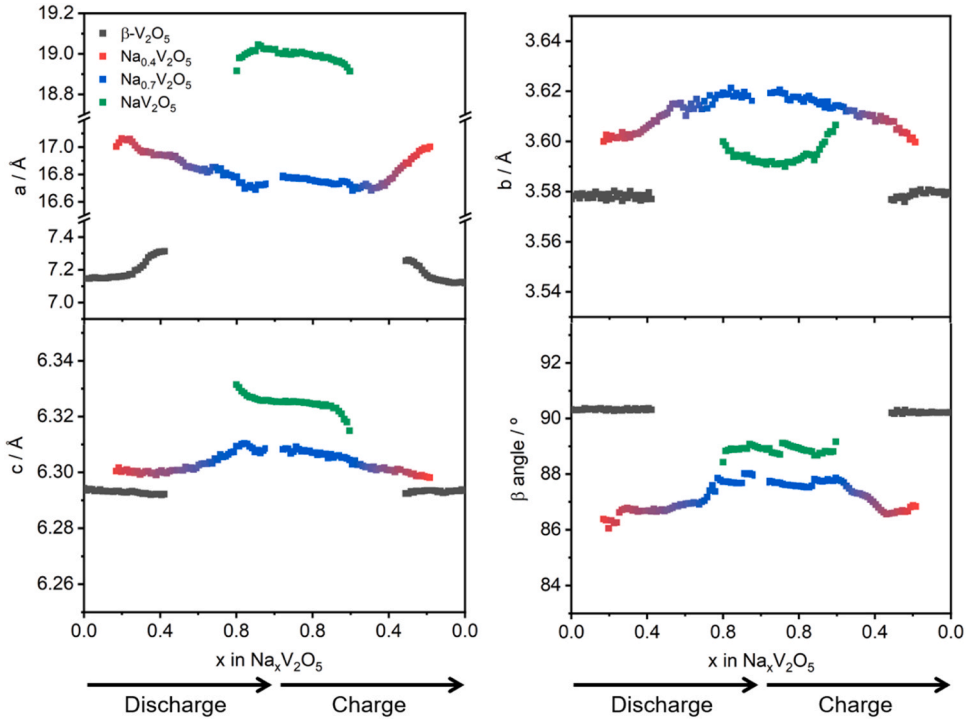

Fig. 10. Evolution of the unit cell parameters of the different sodiated $Na_xV_2O_5$ phases with the sodium content. β-V_2O_5 cell belongs to space group (S. G.) *P* $2_1/m$, while the rest of cells belongs to S. G. *C* 2/*m*.

Table 2
Crystallographic data for selected compositions in the β-$Na_xV_2O_5$ system.

	Space group	Phase	a / Å	b / Å	c / Å	β / °	Interlayer spacing / Å
Discharge	*P* $2_1/m$	β-V_2O_5	7.1363(2)	3.5725(1)	6.2918(1)	90.374(2)	7.14
	C 2/*m*	$Na_{0.4}V_2O_5$	17.0904(5)	3.6088(3)	6.3103(4)	86.503(3)	8.53
		$Na_{0.7}V_2O_5$	16.6911(6)	3.6043(4)	6.3215(4)	87.380(4)	8.34
		NaV_2O_5	19.0506(8)	3.6175(3)	6.3242(8)	88.467(3)	9.54
Charge	*C* 2/*m*	$Na_{0.7}V_2O_5$	16.6328(4)	3.6165(1)	6.3204(5)	87.284(6)	8.29
		$Na_{0.4}V_2O_5$	17.1168(6)	3.6129(7)	6.3200(7)	86.536(5)	8.53
	P $2_1/m$	β-V_2O_5	7.1479(2)	3.56335(5)	6.27202(2)	90.521(6)	7.15

Table S1). The red colored area corresponds to the contribution of the surface charge storage mechanism while the black contour includes the total capacity. At a slow scan rate of 0.02 mV s^{-1} (corresponding to ~22 h per sweep), sodium ions have sufficient time to penetrate the electrode surface and intercalate into the interlayer space, resulting in a greater contribution of faradaic, diffusion-controlled processes (intercalation). However, the surface also contributes to charge storage, although the contribution in as-synthesized β-V_2O_5 is small due to its

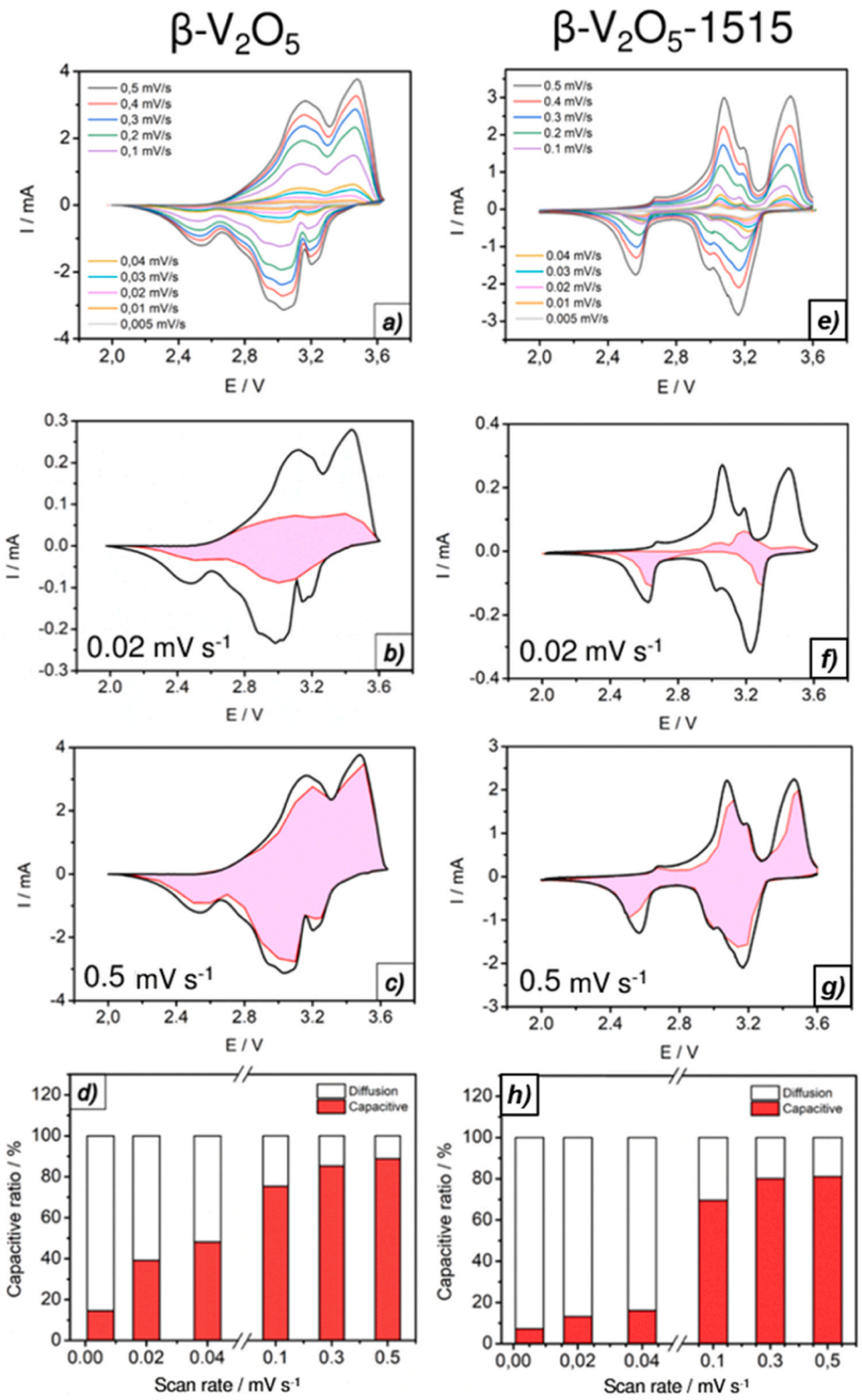

Fig. 11. Left column: as-prepared β-V_2O_5; right column: β-V_2O_5-1515; a) and e) cyclic voltammograms at different scan rates; cyclic voltammograms at b) and f) 0.02 mV s^{-1} and c) and g) 0.5 mV s^{-1} scan rates, where the shaded area in red corresponds to the capacitive charge storage contribution; d) and h) comparison of capacitive and diffusion controlled contributions at low and high scan rates.

low surface area (2.910 m^2 g^{-1}). At high sweep rates, *i.e.* 0.5 mV s^{-1} (corresponding to ~0.9 hours per sweep), sodium ions reaching the surface have less time to diffuse and the contribution of diffusion-controlled faradaic mechanism decreases. At such a fast sweep rate, charge accumulation occurs at the electrode surface. This capacitive process is likely to be characterized by electrochemical adsorption of sodium ions, typical of the surface redox pseudocapacitive mechanism. Fig. 11d compares diffusion and (pseudo)capacitive contributions at different scan rates in as-synthesized β-V_2O_5. The prevalence of the diffusion-controlled faradaic contribution at low rates is remarkable,

while the surface redox (pseudo)capacitive contribution dominates at high scan rates.

As for β-V_2O_5-1515 (Fig. 11e), a similar trend is observed regarding the proportion of surface and diffusion contributions: at low scan rates, the charge storage mechanism is diffusion controlled, while at high scan rates the capacitive contribution dominates (Figs. 11f, 11g and 11h). However, there is a notable difference: faradaic processes contribute more to the charge storage in β-V_2O_5-1515 compared to as-prepared β-V_2O_5, indicating that the diffusion process is more favored in the milled compound compared to as-synthesized β-V_2O_5, which explains its higher capacity at high current rates. This conclusion is endorsed by the analysis of b-value, which also accounts for the increase of the contribution from diffusion processes to the charge storage mechanism after milling the compound (full analysis of b-value can be found in SI, Fig. S6). Considering that β-V_2O_5-1515 has a higher surface area than β-V_2O_5 (3.766 vs 2.910 $m^2\ g^{-1}$), one might expect the opposite, *i.e.* a higher participation of the pseudocapacitive charge storage mechanism as typically observed for extrinsic pseudocapacitive compounds [34]. From this, it can be concluded that the shortening of the diffusion path length has a more important effect by allowing rapid sodiation of the particles. However, since mechanical milling also induces significant lattice defects in layered compounds [35] that could affect diffusion pathways and hence diffusion coefficients, we decided to additionally investigate changes in sodium diffusion coefficient upon milling.

4.5. Kinetics study in as-prepared and milled β-V_2O_5

The kinetics of sodium diffusion was investigated by PEIS in as-prepared β-V_2O_5 and β-V_2O_5-1515. For the former, impedance data were collected close to OCV. For the latter, the EIS experiment was performed in the charged state, i.e. after a complete discharge-charge cycle, due to the scattering of the data in the low frequency range obtained before the first discharge. At OCV and after a single complete cycle, no sodium ions are expected to be in the host. However, the AC perturbation induces sodium intercalation and deintercalation as the sign of the sinusoidal current changes. This assumption is confirmed by the presence of a mass diffusion response under the perturbation. Since the perturbation is small, to ensure that the system remains in linear conditions, the amount of sodium is very small, and the calculated diffusion coefficient is determined under dilute conditions. Under these conditions, only the defects induced during milling influence the observed change in the diffusion coefficient.

Fig. 12 shows the corresponding Nyquist plots, and the insets show the x-intercept of the high frequency data. At medium frequency, the impedance response of both electrodes is a depleted semicircle. In the low frequency range, where the slowest processes take place, a linear relationship between –Im(Z) and Re(Z) appears immediately after the semicircle, which is related to the migration of sodium ions under semi-infinite conditions close to the surface layer, *i.e.* mass diffusion.

The same equivalent circuit was used to fit the impedance data of both as-synthesized V_2O_5 and β-V_2O_5-1515 (Fig. 12a inset), which consists of a typical Randles circuit [36] with the addition of an extra capacitor. This modification has been widely proposed by previous authors [37,38]. Each element of this circuit is associated with a different physicochemical process, thus resulting in a different impedance response: the pure resistor corresponds to the resistance of sodium ions migration through the electrolyte, R_{el}, represented by the x-intercept in the insets of Fig. 12. The depleted semicircle is modelled with an RCPE element (resistor in parallel with CPE), where CPE corresponds to a constant-phase element with a pseudo-capacitance Q, instead of a pure capacitor. According to previous work [39,40], two semicircles would be expected, corresponding to two different electrochemical processes taking place at the electrode-electrolyte interface: i) the migration of sodium ions across the cathode-electrolyte interface (CEI) and the charge accumulation that takes place there, and ii) the charge transfer process (solvation/desolvation of sodium ions) at the electrode-electrolyte interface in parallel with the double layer capacitance. In this case, however, the two semicircles overlap because the two physical phenomena are likely to have very close relaxation frequency values [41]. On the other hand, when modelling impedance data, CPE has been used as an alternative to pure capacitors to account for the relaxation frequency distribution [41], which in the case of electrochemical cells is caused by the non-ideality of the electrode surface and its interface with the electrolyte (irregularities, defects, roughness, etc.). This RCPE element is modelled by R_{tot} and Q_{tot}. R_{tot} corresponds to CEI resistance (R_{int}) and charge transfer process (R_{ct}). Q_{tot} takes into account an electrical double layer pseudocapacitance (Q_{dl}) and the pseudocapacitance associated with the CEI (Q_{int}). In the low frequency range, a straight spike can be observed, which is associated with the semi-infinite diffusion process of sodium ions in the electrode near the surface. In the equivalent circuit, this response is modelled by a Warburg element. The ideal linear relationship between the imaginary and the real parts of the impedance forms an angle of 45° with both axes, *i.e.* both Re(Z) and –Im(Z) have the same value, which is characteristic of a semi-infinite diffusion process. This linear variation deviates from this regime at the very low frequencies. To model this deviation, Q_{acc} is introduced in series in the Randles equivalent circuit. This deviation from the 45° angle accounts for charge accumulation phenomena on the electrode surface due to the limited kinetics of sodium diffusion [38,42]. In Fig. 12, the fit to experimental data is shown by a red line, modelled by the equivalent circuit shown in the inset of Fig. 12, while the fitted parameters are listed in Table 3. The results of the fitted parameters

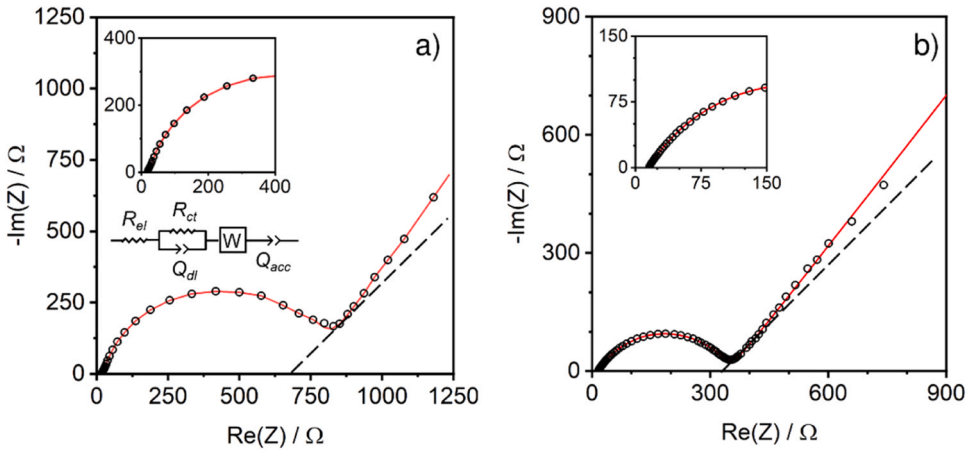

Fig. 12. Nyquist plots corresponding to the impedance of the working electrode made of a) as-prepared β-V_2O_5 and b) β-V_2O_5-1515 at OCV. The insets show an enlarged view of the high frequency region and the equivalent circuit used to fit both spectra. The dashed black line represents a 45° angle, as a reference.

Table 3
Fitted parameters, including resistance, capacitance and exponent *n* indicating the deviation from ideality of the CPE elements for as-prepared β-V_2O_5 and β-V_2O_5-1515.

		β-V_2O_5	β-V_2O_5-1515
R_{el} / Ω mg^{-1}		7.35	4.33
$R_{int} + R_{ct}$ / Ω mg^{-1}		304.5	89.32
CPE_{tot}	Q_{tot} / F s^{n-1}	2.04×10^{-4}	4.87×10^{-6}
	n	0.82	0.65
CPE_{acc}	Q_{acc} / F s^{n-1}	2.85×10^{-2}	3.11×10^{-2}
	n	0.8	0.6

show that R_{tot}, *i.e.* $R_{ct} + R_{int}$, is indeed reduced after the milling process, indicating an improvement in the kinetics of sodium migration through the CEI. It is also interesting to compare the exponent *n,* which describes the behavior of the sodium ion migration process: for a purely diffusive process, $n = 0.5$, while for a purely capacitive behavior, $n = 1$. From the fitted exponent *n* of CPE_{acc}, as well as from the Nyquist plots (regarding the angle deviation from 45°), it can be deduced that in β-V_2O_5-1515, the diffusive processes are more favored than in β-V_2O_5, in agreement with the results obtained from CV experiments at different sweep rates (Figs. 11d and 11h).

The sodium ion diffusion coefficient, D_{Na+}, was calculated using the following equation as described in ref. [36].

$$D_{Na^+} = \left(\frac{V_m}{zFA}\right)^2 \left(\frac{dE}{dx}\right)^2 \left(\frac{1}{\sqrt{2}\ mA_w}\right)^2$$

V_m is the molar volume of β-V_2O_5, *z* is the number of electrons exchanged in the redox reaction, *F* is the Faraday constant, *A* is the specific area determined by the BET method on the pristine β-V_2O_5 and β-V_2O_5-1515 (adsorption-desorption isotherms are shown in Fig. S7), *dE/dx* is the slope of the tangent line to the *E* vs *x* equilibrium curve (Figs. S1 and S8) at the *x* value at which the impedance measurements were made (*i.e.* close to OCV corresponding to a very low sodium content), *m* is the electrode mass, and A_W is the Warburg coefficient, determined from the Warburg element of the impedance data. The A_W value was obtained by reading the minimum of the $-Im(Z)^*\omega^{1/2}$ vs ω plot (Fig. S9), as the Warburg region may partially overlap with adjacent circuit elements (such as RCPE semicircle and Q_{acc} capacitor). At this point of the curve, only the Warburg diffusion process contributes to the impedance response [43]. The resulting D_{Na+} for the studied compounds are 1.78×10^{-13} cm^2 s^{-1} for the as-prepared β-V_2O_5 and 1.73×10^{-11} cm^2 s^{-1} for β-V_2O_5-1515. In addition, the methodology is the same in both cases (unmilled and milled samples) and the D_{Na+} values obtained can then be compared.

Diffusion coefficients are found to be different, although the crystal structure is kept upon milling. However, the milling process not only reduces the particle size of the compound, but also causes the formation of defects mainly on the surface of the particles [35], which may affect the local structure of β-V_2O_5 close to the surface. This change in local structure cannot be detected by XRD, which is particularly difficult to analyze for very small particles due to the significant broadening of reflections. It should be also noted that the values of the Warburg coefficient (A_W) are obtained for the diffusion of sodium ions in a semi-infinite regime, i.e. close to the surface of the particles [44]. For small particles, near-surface diffusion approaches bulk diffusion. On the other hand, sodium diffusion in large particles may be different depending on whether it occurs near the surface or in the bulk. In the latter case, the determined diffusion coefficient is less sensitive to near-surface defects.

β-V_2O_5-1515 has a higher D_{Na+} value (by two orders of magnitude) than as-prepared β-V_2O_5, probably due to near-surface defects, suggesting better kinetics of Na^+ diffusion. The higher D_{Na+} of β-V_2O_5-1515 is consistent with the more diffusive behavior of the charge storage mechanism compared to pristine β-V_2O_5, as deduced from Fig. 11. Furthermore, considering that the diffusion time is given by $t = L^2/D$ (where *L* is the diffusion path length and *D* is the diffusion coefficient) [45,46], a faster migration of Na^+ ions is expected in β-V_2O_5-1515 due to the increase in *D*. Consequently, a better electrochemical performance is obtained for β-V_2O_5-1515, with the difference being more significant at high current rates, as demonstrated by the electrochemical results reported here. Furthermore, the slight reduction in particle size described above (Figs. 1 and 2) also contributes to a quadratic decrease in the time *t* for intercalation and thus, to a significant increase in the sodium (de) insertion rate [47], because the smaller the particles are, the shorter the diffusion path length is. Moreover, the morphological changes induced by mechanical milling result in a higher specific surface area, leading to a larger contact area with the electrolyte and thus, to a higher Na^+ transfer across the interface. Furthermore, the formation of structural and surface defects plays an important role in the diffusion process, as they act as accessible sites on the surface of the active material [44,48].

5. Conclusions

In this work, we report a significant improvement of the electrochemical performance of high-pressure β-V_2O_5 when used as the cathode in sodium batteries. The reversibility of the sodium intercalation/deintercalation is confirmed through *operando* X-ray diffraction. Durability and excellent capacity retention during cycling and at a high current rate have been achieved in sodium half cells by using carbonate-free IL-based NaFSI:Pyr_{13}FSI 1:9 electrolyte and β-V_2O_5 active material with a small particle size (100 – 350 nm), obtained by mechanical milling. This combination not only offers long cyclability but also maintains excellent capacity retention at both slow C/20 (120 mAh g^{-1} at cycle 120) and high 1 C rates (75 mAh g^{-1} at cycle 150).

Mechanical milling not only increases surface area and shortens diffusion paths but also impacts the sodium diffusion coefficient, increasing D_{Na+} by two orders of magnitude, from 1.78×10^{-13} cm^2 s^{-1} to 1.73×10^{-11} cm^2 s^{-1}, as determined by impedance spectroscopy. This increase is likely due to the creation of structural near-surface defects in the layered compound. The synergistic effect of both shorter diffusion paths and enhanced ion diffusion ($t = L^2/D$) explains the significantly improved performance of β-V_2O_5-1515 compared to as-prepared β-V_2O_5. We demonstrate that mechanically reducing particle size in conjunction with appropriate carbonate-free electrolytes is a straightforward strategy to enhance the performance of the β-V_2O_5 cathode material.

The charge storage mechanism in β-V_2O_5-1515 is primarily diffusive, whereas, in pristine β-V_2O_5, capacitive contributions are favored due to limited intercalation, as demonstrated by CV and PEIS experiments. In β-V_2O_5-1515, capacitive processes are significant only at very high current rates, where diffusion/intercalation processes are more restricted. The improved electrochemical results reported here encourage further efforts to overcome the main drawback of β-V_2O_5, which is only available through high-pressure synthesis, thus limiting large-scale production.

CRediT authorship contribution statement

Oleksandr Dolotko: Writing – review & editing, Investigation. **Alois Kuhn:** Writing – review & editing, Writing – original draft, Visualization, Supervision, Methodology, Investigation, Conceptualization. **Flaviano García-Alvarado:** Writing – review & editing, Writing – original draft, Visualization, Supervision, Methodology, Funding acquisition, Conceptualization. **Rafael Córdoba Rojano:** Writing – original draft, Visualization, Investigation.

Declaration of Competing Interest

The authors declare that they have no known competing financial interests or personal relationships that could have appeared to influence the work reported in this paper.

Data Availability

The data that has been used is confidential.

Acknowledgments

We thank MCIN/AEI/10.13039/501100011033 for funding the project PID2022–139039OB-C21. Rafael Córdoba thanks the AEI and European Social Fund/UE for the predoctoral fellowship BES-2017–080862. We also thank José Manuel Gallardo-Amores (High-Pressure Laboratory, Universidad Complutense de Madrid) and María José Torralvo Fernández (Department of Inorganic Chemistry, Universidad Complutense de Madrid) for the synthesis of β-V_2O_5 and BET experiments, respectively.

Appendix A. Supporting information

Supplementary data associated with this article can be found in the online version at doi:10.1016/j.jallcom.2024.175512.

References

[1] N. Yabuuchi, K. Kubota, M. Dahbi, S. Komaba, Research development on sodium-ion batteries, Chem. Rev. 114 (2014) 11636–11682, https://doi.org/10.1021/cr500192f.
[2] R. Berthelot, D. Carlier, C. Delmas, Electrochemical investigation of the P2–Na_xCoO_2 phase diagram, Nat. Mater. 10 (2011) 74–80, https://doi.org/10.1038/nmat2920.
[3] X. Ma, H. Chen, G. Ceder, Electrochemical properties of monoclinic $NaMnO_2$, J. Electrochem Soc. 158 (2011) A1307, https://doi.org/10.1149/2.035112jes.
[4] S. Bach, N. Baffier, J.P. Pereira-Ramos, R. Messina, Electrochemical sodium intercalation in $Na_{0.33}V_2O_5$ bronze synthesized by a sol-gel process, Solid State Ion 37 (1989) 41–49, https://doi.org/10.1016/0167-2738(89)90285-3.
[5] H. Liu, H. Zhou, L. Chen, Z. Tang, W. Yang, Electrochemical insertion/deinsertion of sodium on NaV_6O_{15} nanorods as cathode material of rechargeable sodium-based batteries, J. Power Sources 196 (2011) 814–819, https://doi.org/10.1016/j.jpowsour.2010.07.062.
[6] M. Guignard, C. Didier, J. Darriet, P. Bordet, E. Elkaïm, C. Delmas, P2-Na_xVO_2 system as electrodes for batteries and electron-correlated materials, Nat. Mater. 12 (2013) 74–80, https://doi.org/10.1038/nmat3478.
[7] D. Hamani, M. Ati, J.-M. Tarascon, P. Rozier, Na_xVO_2 as possible electrode for Na-ion batteries, Electrochem Commun. 13 (2011) 938–941, https://doi.org/10.1016/j.elecom.2011.06.005.
[8] S.-W. Kim, D.-H. Seo, X. Ma, G. Ceder, K. Kang, Electrode materials for rechargeable sodium-ion batteries: potential alternatives to current lithium-ion batteries, Adv. Energy Mater. 2 (2012) 710–721, https://doi.org/10.1002/aenm.201200026.
[9] W. Song, X. Cao, Z. Wu, J. Chen, K. Huangfu, X. Wang, Y. Huang, X. Ji, A study into the extracted ion number for NASICON structured $Na_3V_2(PO_4)_3$ in sodium-ion batteries, Phys. Chem. Chem. Phys. 16 (2014) 17681–17687, https://doi.org/10.1039/C4CP01821D.
[10] Y. Lu, L. Wang, J. Cheng, J.B. Goodenough, Prussian blue: a new framework of electrode materials for sodium batteries, Chem. Commun. 48 (2012) 6544–6546, https://doi.org/10.1039/C2CC31777J.
[11] A. Langrock, Y. Xu, Y. Liu, S. Ehrman, A. Manivannan, C. Wang, Carbon coated hollow Na_2FePO_4F spheres for Na-ion battery cathodes, J. Power Sources 223 (2013) 62–67, https://doi.org/10.1016/j.jpowsour.2012.09.059.
[12] H. Zou, S. Li, X. Wu, M.J. McDonald, Y. Yang, Spray-drying synthesis of pure Na_2CoPO_4F as cathode material for sodium ion batteries, ECS Electrochem. Lett. 4 (2015) A53–A55, https://doi.org/10.1149/2.0061506eel.
[13] Y. Zhong, Z. Wu, Y. Tang, W. Xiang, X. Guo, B. Zhong, Micro-nano structure Na_2MnPO_4F/C as cathode material with excellent sodium storage properties, Mater. Lett. 145 (2015) 269–272, https://doi.org/10.1016/j.matlet.2015.01.110.
[14] C. Choi, D.S. Ashby, D.M. Butts, R.H. DeBlock, Q. Wei, J. Lau, B. Dunn, Achieving high energy density and high power density with pseudocapacitive materials, Nat. Rev. Mater. 5 (2020) 5–19, https://doi.org/10.1038/s41578-019-0142-z.
[15] R. Enjalbert, J. Galy, A refinement of the structure of V_2O_5, Acta Crystallogr C. Struct. Chem. 42 (1986) 1467–1469, https://doi.org/10.1107/S0108270186091825.
[16] D. Muller-Bouvet, R. Baddour-Hadjean, M. Tanabe, L.T.N. Huynh, M.L.P. Le, J. P. Pereira-Ramos, Electrochemically formed α'-NaV_2O_5: a new sodium intercalation compound, Electro Acta 176 (2015) 586–593, https://doi.org/10.1016/j.electacta.2015.07.030.
[17] Q.L. Wei, J. Liu, W. Feng, J.Z. Sheng, X.C. Tian, L. He, Q.Y. An, L.Q. Mai, Hydrated vanadium pentoxide with superior sodium storage capacity, J. Mater. Chem. A Mater. 3 (2015) 8070–8075, https://doi.org/10.1039/c5ta00502g.
[18] S. Tepavcevic, H. Xiong, V.R. Stamenkovic, X.B. Zuo, M. Balasubramanian, V. B. Prakapenka, C.S. Johnson, T. Rajh, Nanostructured bilayered vanadium oxide electrodes for rechargeable sodium-ion batteries, ACS Nano 6 (2012) 530–538, https://doi.org/10.1021/nn203869a.
[19] Y. Li, J. Ji, J. Yao, Y. Zhang, B. Huang, G. Cao, Sodium ion storage performance and mechanism in orthorhombic V_2O_5 single-crystalline nanowires, Sci. China Mater. 64 (2021) 557–570, https://doi.org/10.1007/s40843-020-1468-6.
[20] L.Y. Su, J. Winnick, P. Kohl, Sodium insertion into vanadium pentoxide in methanesulfonyl chloride-aluminum chloride ionic liquid, J. Power Sources 101 (2001) 226–230, https://doi.org/10.1016/S0378-7753(01)00787-X.
[21] R. Baddour-Hadjean, M.S. Renard, J.P. Pereira-Ramos, Enhanced electrochemical properties of ball-milled gamma '-V_2O_5 as cathode material for Na-ion batteries: a structural and kinetic investigation, J. Power Sources 482 (2021), https://doi.org/10.1016/j.jpowsour.2020.229017.
[22] J.M. Cocciantelli, P. Gravereau, J.P. Doumerc, M. Pouchard, P. Hagenmuller, On the preparation and characterization of a new polymorph of V_2O_5, J. Solid State Chem. 93 (1991) 497–502, https://doi.org/10.1016/0022-4596(91)90323-A.
[23] R. Baddour-Hadjean, M.S. Renard, N. Emery, L.T.N. Huynh, M.L.P. Le, J.P. Pereira-Ramos, The richness of V_2O_5 polymorphs as superior cathode materials for sodium insertion, Electro Acta 270 (2018) 129–137, https://doi.org/10.1016/j.electacta.2018.03.062.
[24] F. García-Alvarado, J.M. Tarascon, B. Wilkens, Synthesis and electrochemical study of new copper vanadium bronzes and of 2 new V_2O_5 polymorphs - beta'-V_2O_5 and epsilon'-V_2O_5, J. Electrochem Soc. 139 (1992) 3206–3214, https://doi.org/10.1149/1.2069054.
[25] M.E. Arroyo-de Dompablo, J.M. Gallardo-Amores, U. Amador, E. Morán, Are high pressure materials suitable for electrochemical applications? HP-V_2O_5 as a novel electrode material for Li batteries, Electrochem Commun. 9 (2007) 1305–1310, https://doi.org/10.1016/j.elecom.2007.01.035.
[26] R. Trócoli, P. Parajuli, C. Frontera, A.P. Black, G.C.B. Alexander, I. Roy, M. E. Arroyo-de Dompablo, R.F. Klie, J. Cabana, M.R. Palacín, β-V_2O_5 as magnesium intercalation cathode, ACS Appl. Energy Mater. (2022), https://doi.org/10.1021/acsaem.2c02371.
[27] R. Córdoba, A. Kuhn, J.C. Pérez-Flores, E. Morán, J.M. Gallardo-Amores, F. García-Alvarado, Sodium insertion in high pressure β-V_2O_5: a new high capacity cathode material for sodium ion batteries, J. Power Sources 422 (2019) 42–48, https://doi.org/10.1016/j.jpowsour.2019.03.018.
[28] R. Córdoba, J. Goclon, A. Sarapulova, Q. Fu, J. Maibach, S. Dsoke, F. Fauth, A. Kuhn, F. García-Alvarado, From high-pressure β-V_2O_5 to κ-$Na_xV_2O_5$ (x = 0.4 – 0.55): a structural, chemical and kinetic insight into a sodiated phase with a large interlayer space, Appl. Res. (2022), https://doi.org/10.1002/appl.202200052.
[29] V.P. Filonenko, M. Sundberg, P.-E. Werner, I.P. Zibrov, Structure of a high-pressure phase of vanadium pentoxide, β-V_2O_5, Acta Crystallogr. Sect. B 60 (2004) 375–381, https://doi.org/10.1107/S0108768104012881.
[30] J. Rodríguez-Carvajal, Recent advances in magnetic structure determination by neutron powder diffraction, Phys. B Condens Matter 192 (1993) 55–69, https://doi.org/10.1016/0921-4526(93)90108-I.
[31] M. Herklotz, J. Weiß, E. Ahrens, M. Yavuz, L. Mereacre, N. Kiziltas-Yavuz, C. Dräger, H. Ehrenberg, J. Eckert, F. Fauth, L. Giebeler, M. Knapp, A novel high-throughput setup for in situ powder diffraction on coin cell batteries, J. Appl. Crystallogr 49 (2016) 340–345, https://doi.org/10.1107/S1600576715022165.
[32] P. Sharma, C. Das, S. Indris, T. Bergfeldt, L. Mereacre, M. Knapp, U. Geckle, H. Ehrenberg, M.S.D. Darma, Synthesis and characterization of a multication doped Mn spinel, $LiNi_{0.3}Cu_{0.1}Fe_{0.2}Mn_{1.4}O_4$, as 5 V positive electrode material, ACS Omega 5 (2020) 22861–22873, https://doi.org/10.1021/acsomega.0c02174.
[33] K. Pfeifer, S. Arnold, J. Becherer, C. Das, J. Maibach, H. Ehrenberg, S. Dsoke, Can metallic sodium electrodes affect the electrochemistry of sodium-ion batteries? Reactivity issues and perspectives, ChemSusChem 12 (2019) 3312–3319, https://doi.org/10.1002/cssc.201901056.
[34] V. Augustyn, P. Simon, B. Dunn, Pseudocapacitive oxide materials for high-rate electrochemical energy storage, Energy Environ. Sci. 7 (2014) 1597–1614, https://doi.org/10.1039/C3EE44164D.
[35] J. Qu, L. Sha, C. Wu, Q. Zhang, Applications of mechanochemically prepared layered double hydroxides as adsorbents and catalysts: a mini-review, Nanomaterials 9 (2019), https://doi.org/10.3390/nano9010080.
[36] C. Ho, I.D. Raistrick, R.A. Huggins, Application of A-C techniques to the study of lithium diffusion in tungsten trioxide thin films, J. Electrochem Soc. 127 (1980) 343–350, https://doi.org/10.1149/1.2129668.
[37] M. Casas-Cabanas, V. v Roddatis, D. Saurel, P. Kubiak, J. Carretero-González, V. Palomares, P. Serras, T. Rojo, Crystal chemistry of Na insertion/deinsertion in $FePO_4$–$NaFePO_4$, J. Mater. Chem. 22 (2012) 17421–17423, https://doi.org/10.1039/C2JM33639A.
[38] K. Adams, A.F. González, J. Mallows, T. Li, J.H.J. Thijssen, N. Robertson, Facile synthesis and characterization of $Bi_{13}S_{18}I_2$ films as a stable supercapacitor electrode material, J. Mater. Chem. A Mater. 7 (2019) 1638–1646, https://doi.org/10.1039/C8TA11029H.
[39] Y. Chang, H. Sohn, Electrochemical impedance analysis for lithium ion intercalation into graphitized carbons, J. Electrochem Soc. 147 (2000) 50, https://doi.org/10.1149/1.1393156.
[40] M. Dollé, F. Orsini, A.S. Gozdz, J.-M. Tarascon, Development of reliable three-electrode impedance measurements in plastic Li-ion batteries, J. Electrochem Soc. 148 (2001) A851, https://doi.org/10.1149/1.1381071.
[41] J.-I. Yamaura, M. Isobe, H. Yamada, T. Yamauchi, Y. Ueda, Low temperature X-ray study of β-$A_xV_2O_5$, J. Phys. Chem. Solids 63 (2002) 957–960, https://doi.org/10.1016/S0022-3697(02)00082-3.
[42] D.J. Kim, R. Ponraj, A.G. Kannan, H.-W. Lee, R. Fathi, R. Ruffo, C.M. Mari, D. K. Kim, Diffusion behavior of sodium ions in $Na_{0.44}MnO_2$ in aqueous and non-

aqueous electrolytes, J. Power Sources 244 (2013) 758–763, https://doi.org/10.1016/j.jpowsour.2013.02.090.
[43] H. Anne, Understanding the kinetic limitations of $NaFePO_4$ as cathode active material for Na-ion batteries, Universidad del País Vasco, 2019.
[44] R. Malik, D. Burch, M. Bazant, G. Ceder, Particle size dependence of the ionic diffusivity, Nano Lett. 10 (2010) 4123–4127, https://doi.org/10.1021/nl1023595.
[45] P.G. Bruce, B. Scrosati, J.-M. Tarascon, Nanomaterials for rechargeable lithium batteries, Angew. Chem. Int. Ed. 47 (2008) 2930–2946, https://doi.org/10.1002/anie.200702505.
[46] A.S. Arico, P. Bruce, B. Scrosati, J.-M. Tarascon, W. van Schalkwijk, Materials for sustainable energy: a collection of peer-reviewed research and review articles from Nature Publishing Group, World Scientific, 2011.
[47] H. Liu, J. Wang, X. Zhang, D. Zhou, X. Qi, B. Qiu, J. Fang, R. Kloepsch, G. Schumacher, Z. Liu, J. Li, Morphological evolution of high-voltage spinel $LiNi_{0.5}Mn_{1.5}O_4$ cathode materials for lithium-ion batteries: the critical effects of surface orientations and particle size, ACS Appl. Mater. Interfaces 8 (2016) 4661–4675, https://doi.org/10.1021/acsami.5b11389.
[48] M. Park, X. Zhang, M. Chung, G.B. Less, A.M. Sastry, A review of conduction phenomena in Li-ion batteries, J. Power Sources 195 (2010) 7904–7929, https://doi.org/10.1016/j.jpowsour.2010.06.060.